Journal of Mechanics Engineering and Automation 4 (2014) 887-899

External Weather Data Assimilation to Simulate Wind and Temperature Fields in the Region of Gualeguaychú, Argentina

César Augusto Aguirre[1, 3], Guillermo Jorge Berri[2], Armando Benito Brizuela[1, 3] and Emiliana Elisabet Orcellet[2]

1. CICyTTP—CONICET (Centro de Investigaciones Científicas y Transferencia Tecnológica a la Producción—Consejo Nacional de Investigaciones Científicas y Técnicas), UADER (Universidad Autónoma de Entre Ríos), Diamante 3105, Argentina

2. SMN (Servicio Meteorológico Nacional), CONICET (Consejo Nacional de Investigaciones Científicas y Técnicas), Buenos Aires 1002, Argentina

3. FCA—UNER (Facultad de Ciencias Agropecuarias—Universidad Nacional de Entre Ríos), Oro Verde 3101, Argentina

Received: July 17, 2014 / Accepted: July 29, 2014 / Published: November 25, 2014.

Abstract: This work shows the comparison between the results of wind and temperature simulation and data weather measurements in low layers near Gualeguaychú City, Argentine, for 12 h in January 1, 2011. The model ARPS (advanced regional prediction system) with two options in the boundary conditions is used. In such conditions, wave-radiating open (radiative) with relaxation to the initial state were used while otherwise used absorbing boundary conditions data forced from MBLM (meso-scale boundary layer model) operational forecasters used by the National Weather Office. The results of both simulations are compared with data measured by three weather stations located around of the Uruguay River. As both simulations are initialized using the same data, there is a better agreement between the values obtained by forcing the boundary conditions for which are using "radiative" boundary conditions after 2 h physical time from the start of the simulation.

Key words: External boundary conditions assimilation, large eddy simulation, atmospheric boundary layer.

1. Introduction

For several decades, it has increased the use of systems of high performance computing to simulate future scenarios in forecasting weather events thanks to the quick progress that has microprocessors and software evolution. Many products derived from observations of meteorological sensors mounted on satellites and observation of natural resources are freely available databases of specialized centers administering these data via the internet. Furthermore, these available databases to the results of numerical modeling global weather variables predicted 96 h with good reliability. However, the spatial resolution of these is too low for use in certain applications that require greater precision, such as air pollution events caused by gas emissions from power plants, industrial parks, urban centers, open dumps, and so on. An alternative to solving this problem is the use of CFD (computational fluid dynamics) codes that allow obtaining results of scalar and vector fields of meteorological variables with a spatial resolution according to the required by the user. Among the CFD, the ARPS (advanced regional prediction system) originally developed by the University of Oklahoma and the CAPS (center for analysis and prediction of storms) in the United States can be used. This code is written in Fortran 90 and the source codes are available online (http://www.caps.ou.edu). This code

Corresponding author: César Augusto Aguirre, Ph.D., professor, research fields: computational fluid dynamics, atmospheric environment, non-renewable energy, geographic information system. E-mail: cesaraguirredalotto@gmail.com.

is very comprehensive as it not only simulates the wind field, but also has models of heat and water fluxes at the soil-atmosphere interface, simulates cloud formation, precipitation and other meteorological phenomena. New algorithm was added to this code for simulating the transport and dispersion of chemically reactive species by coupling a stochastic Lagrangian model [1]. In subsequent work, several validations were performed with the code results of experimental wind tunnel measurements [2, 3]. To validate the code in a real scale, the results of the simulated the wind and temperature fields into atmospheric boundary layer for a summer day near the Gualeguaychú City were presented [4] using wave-radiation open boundary conditions with relaxed towards the base state value of the variables [5]. These results were compared with the measured data for three weather stations. It suggests that while the temperature field is well simulated by the model, the wind must be corrected and taking into account the wind circulation changes outside the computational domain. In this paper, data assimilation wind, temperature and atmospheric pressure are introduced from the MBLM (meso-scale boundary layer model) operating [6, 7]. The wind and temperature fields simulation in lower layers for a summer day in the near cellulose pulp mill UPM-Kimmene (ex-Botnia) region are carried out.

The paper is organized as follows: Section 2 presents the theoretical framework of LES (large eddy simulation), the numerical scheme and closure strategy for SGS (sub-grid scale), the model variables, equations and the forced external data assimilation technique; Section 3 describes the case study, details of the numerical simulation, data source of the initial conditions and external edge condition; Section 4 presents the results of the wind and temperature fields simulated and compared with data measured by three weather stations on two height levels (10 m and 40 m). Two simulations are analyzed: the first simulation is mentioned in Ref. [4], which only took into account the initial conditions of the ground surface (soil temperature, water, topography and vegetation) and aerological data from a radiosonde measurements of Ezeiza City used to initialize the meteorological variables in the atmosphere. The second simulation not only takes into account the initial conditions as the first one, but also the details of the wind field, temperature and atmospheric pressure at the edges of the survey area forced from MBLM model to account changes in wind circulation outside the domain of study during the course of the day; Section 5 presents discussions; and Section 6 gives conclusions and future works.

2. Methods

2.1 The LES of Turbulent Flows

The ARPS code solves the mass balance, momentum, energy equations, and uses the moist air state equation to solve the pressure one [8]. This model has been specifically designed for the monitoring and description of storms. It has sub-models for heat flux and water vapor, cloud formation and precipitation. In order to do so, it takes into account the orography and land cover, as well as initial conditions of the soil and the state of the atmosphere. It is a semi-compressible model, since it considers that the air density only varies with the height in mass balance, momentum, and scalar transport equations but allows compressible treatment in solving the pressure equation using a second time step smaller than for the above equations. That is to say, this code works with two time steps, the larger one for the balance equations and the smaller one to solve the pressure equation. The mass balance, momentum and energy equations are solved using a finite difference scheme, centered in a Arakawa C-grid cell, and uses a curvilinear coordinate system that follows the unevenness of the surface. The numeric scheme used to obtain the solution of the differential equations integrated in the larger time step is a centered, explicit 4° order, while the one used to

integrate the pressure and vertical component of air speed equations is a Crank-Nicholson implicit scheme. Some modifications introducing the option of calculation of the Smagorinsky coefficient [9], following Germano technique [10] in the non-linear term of the momentum balance and scalar transport equations were made [2].

2.2 ARPS Model Variables

Considering a base state and the deviations from the base state, the Reynolds decomposition of the flow in the atmospheric boundary layer and the others scalar magnitudes is proposed. The base state is assumed to be horizontally homogeneous, time invariant and hydrostatically balanced. The base state depends only on the height, while the deviations are three-dimensional variables that evolve with time:

$$\begin{cases} u(x,y,z,t) = \overline{u}(z) + u'(x,y,z,t), \\ v(x,y,z,t) = \overline{v}(z) + v'(x,y,z,t), \\ w(x,y,z,t) = w'(x,y,z,t), \\ \theta(x,y,z,t) = \overline{\theta}(z) + \theta'(x,y,z,t), \\ p(x,y,z,t) = \overline{p}(z) + p'(x,y,z,t), \\ \rho(x,y,z,t) = \overline{\rho}(z) + \rho'(x,y,z,t), \\ q_v(x,y,z,t) = \overline{q_v}(z) + q'_v(x,y,z,t), \\ q_{li}(x,y,z,t) = q'_{li}(x,y,z,t), \\ q_h(x,y,z,t) = q'_h(x,y,z,t). \end{cases} \quad (1)$$

In Eq. (1), u, v and w are, respectively, the three components of the speed field in the three orthogonal Cartesian axes, where x direction is west-east, y direction is south-north and z direction is vertical. Besides, θ is potential temperature, p is pressure, ρ is air density, q_v is the water vapor mixing ratio, q_{li} is water in its liquid state, and q_h is water in its solid state. It can also be observed that the vertical component of the base state of speed is zero ($\overline{w}(z) = 0$).

2.3 The Governing Equations of ARPS Model

The LES technique implies the solving of the turbulent flow scales larger than a Δ scale, which should be in the inertial range of Kolmogorov energy cascade. This involves the use of a spatial filtering operation with a low-pass filter:

$$\vec{u}^{\oplus}(\vec{x},t) = \int_V u(\vec{x}-\vec{r},t)\,G(\vec{r})\,\mathrm{d}\vec{r} \quad (2)$$

where, $\vec{r}$ is radius position vector and $G(\vec{r})$ is the convolution function that meets with the condition: $\int_V G(\vec{r})\mathrm{d}\vec{r} = 1$.

This filtering operation applied in the speed field can be seen as a decomposition of it in large scales $\vec{u}^{\oplus}$ (solved by LES) and the residual small scales $\vec{u}^{\Theta}$ (unsolved):

$$\vec{u}(\vec{x},t) = \vec{u}^{\oplus}(\vec{x},t) + \vec{u}^{\Theta}(\vec{x},t) \quad (3)$$

The filtering operation applied to the mass transfer, momentum and energy equations results in:

$$\frac{\partial\left(\overline{\rho}u_i^{\oplus}\right)}{\partial x_i} = 0 \quad (4)$$

$$\frac{\partial\left(\overline{\rho}u_i^{\oplus}\right)}{\partial t} + \frac{\partial(\overline{\rho}u_i^{\oplus}u_j^{\oplus})}{\partial x_j} = \overline{\rho}g_i B^{\oplus} - \left(\frac{\partial p'}{\partial x_i}\right)^{\oplus} + 2\in_{ijk}\Omega_j\overline{\rho}u_k^{\oplus} - \frac{\partial\left(\overline{\rho}\tau_{ij}\right)}{\partial x_j} + \frac{\partial\left(\overline{\rho}T_{ij}\right)}{\partial x_j} \quad (5)$$

$$\frac{\partial\left(\overline{\rho}\theta^{\otimes}\right)}{\partial t} + \frac{\partial\left(\overline{\rho}u_j^{\oplus}\theta^{\oplus}\right)}{\partial x_j} = S_\theta - \frac{\partial\left(\overline{\rho}h_{\theta_j}\right)}{\partial x_j} \quad (6)$$

In Eqs. (4)-(6), the Gibbs notation are used. S_θ represents the source or sink of the scalar θ, $\overline{\rho}$ represents the average value of air density in the horizontal planes. That is to say that it only varies in altitude (hence, the semi-compressible characteristic of the code). This implies that it was used the following approximation:

$$\rho'(x,y,z,t) << \overline{\rho}(z) \quad (7)$$

Besides, in Eq. (5), B is the total buoyancy, Ω is the angular velocity of the earth, in terms of the Coriolis force, and T_{ij} is the stress tensor of molecular viscosity. In Eqs. (5) and (6), it was used the Leonard identity [11] in the following way:

In the momentum conservation Eq. (5):

$$\begin{aligned} \left(u_i u_j\right)^{\oplus} &= \left(u_i^{\oplus}u_j^{\oplus}\right)^{\oplus} + \left(u_i^{\oplus}u_j^{\Theta} + u_i^{\Theta}u_j^{\oplus}\right)^{\oplus} + \left(u_i^{\Theta}u_j^{\Theta}\right)^{\oplus} \\ &= \left(u_i^{\oplus}u_j^{\oplus}\right) + L_{ij} + C_{ij} + R_{ij} \\ &= \left(u_i^{\oplus}u_j^{\oplus}\right) + \tau_{ij} \end{aligned} \quad (8)$$

while in the energy conservation Eq. (6):

$$\left(u_j\theta\right)^{\oplus} = \left(u_j^{\oplus}\theta^{\oplus}\right)^{\oplus} + h_{\theta_j} \tag{9}$$

In order to solve the stress tensor of sub-grid tensions or sub-grid viscosity τ_{ij} and the $h_{\theta j}$ term, original ARPS has three alternatives: one is to use a gradient model from solved scales, named Standard Smagorinsky model [9]; the second option is to estimate the sub-grid TKE (turbulence kinetic energy) (1.5 TKE), using a transport equation where the terms of production, diffusion, gravity and dissipation are obtained from gradient models [12]; the third alternative has been introduced into the ARPS model [2]. This consists in using the Dynamic Smagorinsky model, following Germano technique [10].

As said before, the pressure equation is solved from the state equation of moist air:

$$\left(\frac{\partial p'}{\partial t}\right)^{\oplus} = -\left(u_i\frac{\partial p'}{\partial x_i}\right)^{\oplus} - g_i\overline{\rho}u_i^{\oplus} - V_s^2\frac{\partial\left(\overline{\rho}u_i\right)^{\oplus}}{\partial x_i} + V_s^2\overline{\rho}\left(\frac{1}{\theta}\frac{\partial\theta}{\partial t} - \frac{1}{A}\frac{\mathrm{d}A}{\mathrm{d}t}\right)^{\oplus} \tag{10}$$

In Eq. (10), V_s represents the speed of sound, and A is the relationship between the constant of ideal gases for dry air and humid air [13]. The term of correlation speed-gradient of the pressure fluctuation is solved using a gradient model [12]. For the formulation of this last equation, it has not been made the semi-compressible characteristic of the model approximate to Eq. (7).

The wall model that allows estimating the tangential tensions $\tau_{13|p}$ and $\tau_{23|p}$ in the cells of the calculation grid closer to the ground is a logarithmic law of the wall:

$$\begin{cases} \tau_{13}|_p = & -\overline{\rho}C_{dm}\left|V_p^{\oplus}\right|u_p^{\oplus} \\ \tau_{23}|_p = & -\overline{\rho}C_{dm}\left|V_p^{\oplus}\right|v_p^{\oplus} \end{cases} \tag{11}$$

where, sub-index p is the value of the variable evaluated at the lowest grid level above ground surface, $\left|V_p^{\oplus}\right|$ is the large-eddy wind speed at the same level and C_{dm} is the friction coefficient calculated bearing in mind the logarithmic wind profile law:

$$C_{dm} = \frac{k_v^2}{\ell n^2\left(\frac{\Delta z_p}{z_0}\right)} \tag{12}$$

where, k_v represents the *Von-Kármán* constant, Δz_p is the height of the calculation cell adjacent to the ground, and z_0 is the soil roughness parameter.

2.4 Boundary Conditions Assimilation from the Regional Prediction Model MBLM

The boundary conditions refer to the values that the simulated variables have by the model out of the domain of the study. These can be of the *Neumann* (zero normal gradients) type, which impose that they are not modified when the flow goes through the boundary of grid. In this model, it also can be used conditions of the "radiative" (wave-radiating open) type that allows softening certain pressure waves in the boundaries of the domain of the simulation, to avoid the reflection and re-entering into it. This kind of condition can be valid for short periods of time (to 1-2 h physical time of simulation) with persistent wind from one direction and moderate speed. However, if it is wanted to simulate longer periods of time (days), the direction and wind speed out of the field of study can vary, hence, it is necessary to assimilate external boundary conditions to take into account these variations in the domain of the simulation. This work shows the way in which the speed and direction of wind assimilation from an operative prediction model used by MBLM is made. This model is, in turn, conditioned to a regional scale from the ETA-CPTEC model (Brazilian Center for Weather Forecasting and Climate Research). For this purpose, the outputs of speed and wind direction, pressure and potential temperature values of the MBLM, which are organized in a spatial resolution grid of 1 km/h for a day, are used. These conditions are imposed in the boundaries of the field of study, using a relaxation function to avoid strong spatial

discontinuities and instabilities in the numerical resolution of Eqs. (4)-(6), (8)-(11).

$$\frac{\partial \varphi}{\partial t} = -K_b\left(\varphi - \varphi_e\right) \tag{13}$$

These terms are added to the mass balance, momentum and energy equations solved by ARPS. In Eq. (13), ϕ represents the value that takes a variable in the calculation domain, while ϕ_e is the external value imposed by the MBLM. Since this equation is solved for all the time steps of the simulation (Δt = 10 s) and ϕ_e is only available every 3,600 s, making a temporal linear interpolation to obtain the external boundary conditions in every time step of the simulation.

The relaxation coefficient K_b is defined as:

$$K_b = \begin{cases} \dfrac{K_{b0}}{1+\left[\dfrac{2\left(i-i_b\right)}{\left(n_b-1\right)}\right]^2} & \text{for } \left|i-i_b\right| \le n_b - 1 \\ 0 & \text{for } \left|i-i_b\right| > n_b - 1 \end{cases} \tag{14}$$

where, K_{b0} is the maximum value of the relaxation coefficient adopted in the boundary, and n_b is the width of the relaxation zone in the simulation grid cell units (i indicates cell position in the grid, and i_b indicates cell position in the relaxation zone). This condition causes the values of the variables close to the calculation domain boundaries, tending to be similar to the values impose by the boundaries of it.

The maximum value of relaxation K_{b0} is chose on the basis of the time steps, considered in the simulation as $10\Delta t \le (K_{b0})^{-1} \le 20\Delta t$. In this simulation, it was used as $K_{b0} = 0.005\ s^{-1}$.

3. Case of Study

3.1 Description of Study Area

The area of study comprises the Argentinean and Uruguayan bank of the Uruguay River, near Gualeguaychú, Argentina and Fray Bentos Uruguay cities. In this area, there are three weather stations in the Argentinean bank of the river. They are indicated as north tower, east tower and south tower in Fig. 1. The stations belong to the Environmental Monitoring Plan of the Uruguay River, developed by the Argentinean National Weather Service, by means of an agreement with the national secretariat of environment and sustainable development. The stations have wind and temperature sensors in two levels: at 2 m and at 40 m for temperature; at 10 m and 40 m for speed and wind direction. In this research, the simulation of wind, temperature, humidity and pressure fields using the ARPS model, was made. The simulation corresponded to the date January 1, 2011, between 9 a.m. and 9 p.m. (12:00 UTC to 24:00 UTC).

3.2 Simulation Description

The simulations had been made using a personal computer with an Intel Pentium dual-core processor and 4 GB RAM. All variables were calculated simulating 12 h/s with the ARPS model (between 9 a.m. and 9 p.m.). The grid is formed by regular prismatic cells of variable height. They had a horizontal dimension of 1 km × 1 km and their height goes from 5 m, for the ground adjacent cells, and as far as 198 m for the ones in the top of the calculation domain.

The variation of height law of the cells follows a hyperbolic tangent function. In this way, the grid is composing of 75 × 75 cells in a horizontal direction,

Fig. 1 Study area and location of automatic weather towers.

and 33 cells in vertical direction. The useful domain height was fixed in 2,150 m, over which it was set a supplementary layer of 990 m (five cells) in order to eliminate the pressure waves using a Rayleigh type shock absorber. It is important to highlight that the vertical coordinate of the grid follows the ground unevenness. Fig. 2 presents a cross section in a west-east direction at UPM-Kimmene pulp mill location.

A time step (Δt_G = 10 s) was used to solve the mass balance, momentum and energy equations while for the pressure equation, a time step is Δt_p = 1 s. These values were adopted as the following expressions:

For the larger time step:

$$\Delta t_G \leq \frac{1}{\left|V_{h,\max}\right|}\left[\left(\frac{1}{\Delta x}\right)^2+\left(\frac{1}{\Delta y}\right)^2\right]^{-\frac{1}{2}} \quad (15)$$

where, $\left|V_{h,\max}\right| = 50$ m·s^{-1} represents the maximum value considered for wind speed, allowing that the solution diverge in the calculation and it is necessary to reduce the time step. Δx = 1,000 m and Δy = 1,000 m are the horizontal spatial dimensions of the calculation grid cell.

For the small time step:

$$\Delta t_p \leq \frac{1}{c_s}\left[\left(\frac{1}{\Delta x}\right)^2+\left(\frac{1}{\Delta y}\right)^2+\left(\frac{1}{\Delta z_{\min}}\right)^2\right]^{-\frac{1}{2}} \quad (16)$$

where, c_s represents the pressure wave speed and it is calculated as:

$$c_s = \sqrt{\frac{\gamma \mathrm{R}\overline{T}}{M}} \quad (17)$$

In Eq. (17), γ = 1.4 is the adiabatic coefficient of air, $\overline{T}$ is the temperature of the base state (K), R = 8.314 J·mol^{-1}·K^{-1} is the universal gas constant, and M = 0.029 kg.mol^{-1} is the molar mass of air. With $\overline{T}$ = 40 °C, Eq. (17) is done with c_s = 354.5 m·s^{-1}.

In Eq. (16), $\Delta z_{\min}$ = 5 m is the minor vertical dimension of the grid cells, but in this case it was not taken into account since it was chose an implicit resolution in vertical direction for speed. With these time steps, the simulations took two hours twenty five minutes for twelve hours' physic-time.

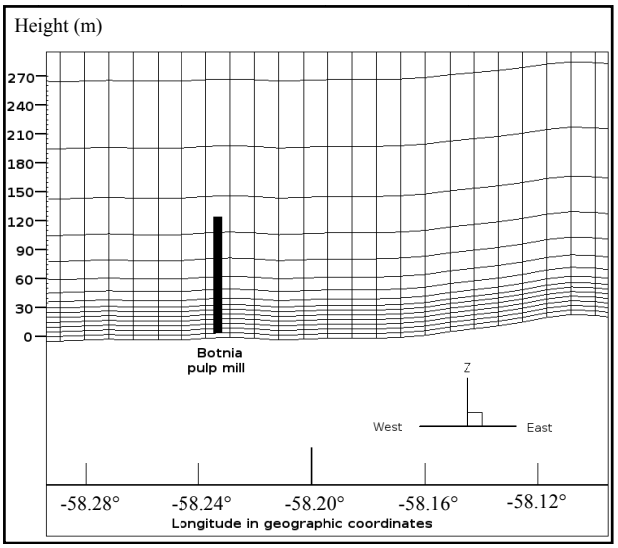

Fig. 2 Cross section in a west-east direction of vertical grid.

3.3 Data Sources for the Initial Conditions

With ARPS, it can be used data of the ground surface characteristics to be included as initial conditions. These data were obtained from the image processing of the LANDSAT 5 and TERRA satellites, for January 1, 2011. With these data, it was proceeded to make a non supervised classification in six categories of the existent elements of the study field (Fig. 3). Afterwards, each category was identified with a field sampling. The sensor's thermal infrared band allowed obtaining data of ground surface temperature (Fig. 4).

The DEM (digital elevation model) showed in Fig. 5 was obtained from the USGS (United States Geological Survey) database (http://srtm.usgs.gov). From the classified image, data of land cover were obtained, like types of vegetation in rural areas, urban areas, and areas covered with water. These kinds of vegetations were categorized according to Olson's World Ecosystem Classes [14] (Fig. 6) and from the correspondence proposed by the authors, and the soil roughness parameter map (Fig. 7) was obtained.

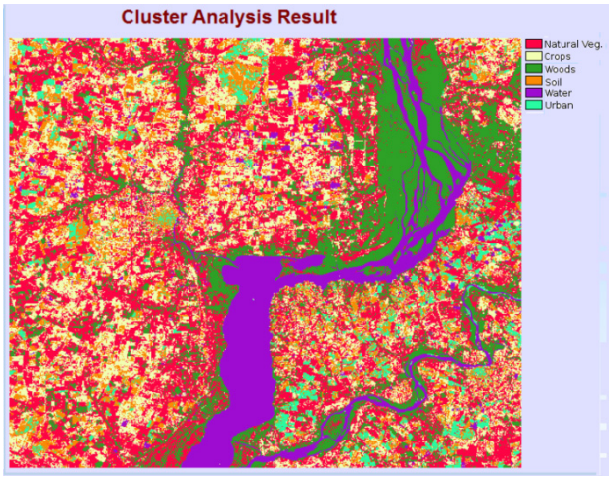

Fig. 3 Cluster classification of ground cover.

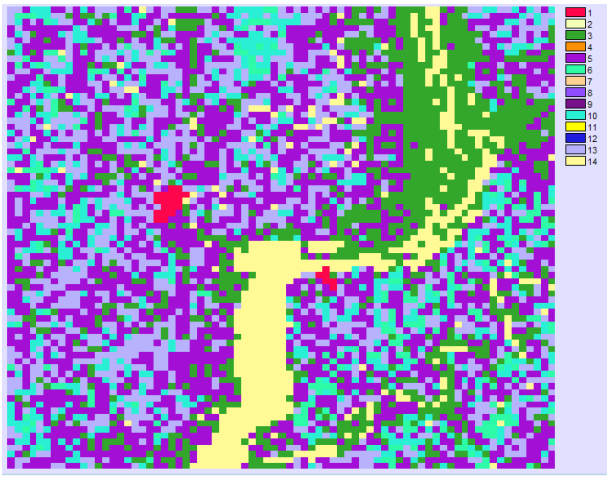

Fig. 6 Vegetation type.

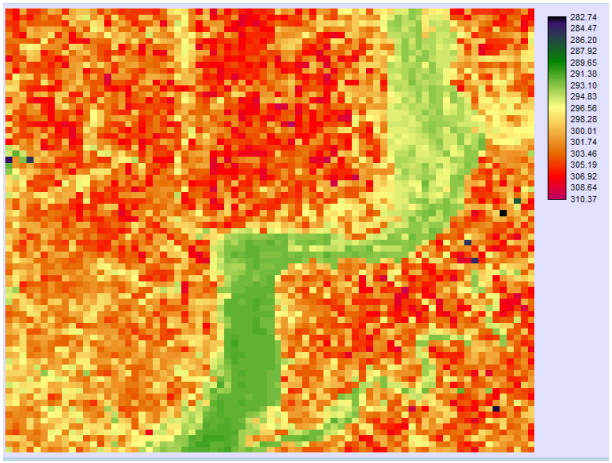

Fig. 4 Ground surface temperature (K).

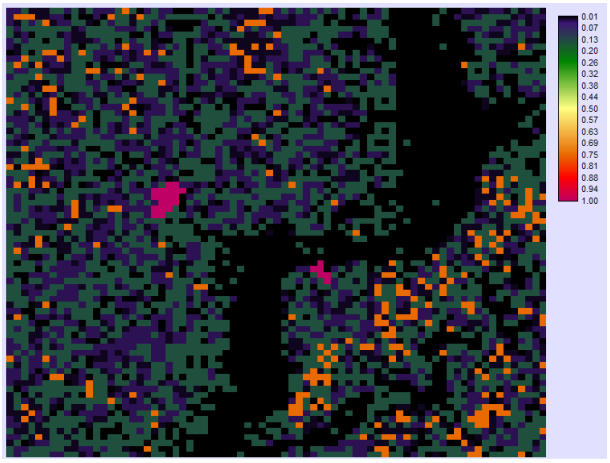

Fig. 7 Roughness parameter.

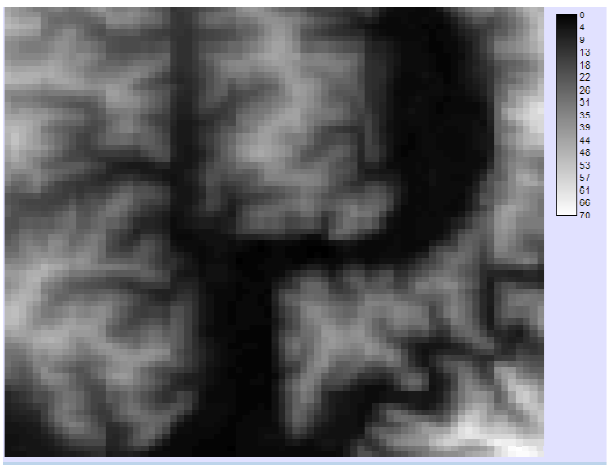

Fig. 5 Digital elevation model (m).

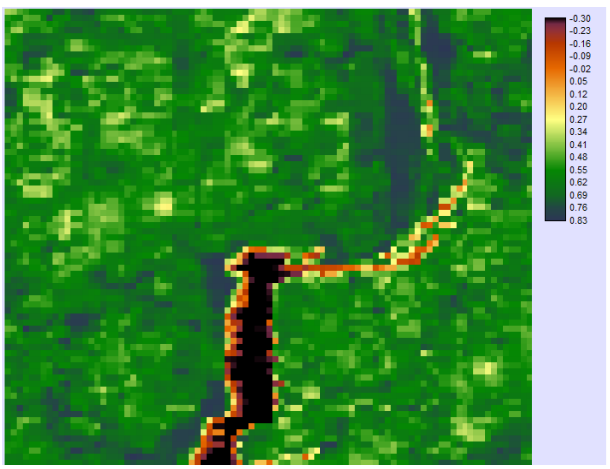

Fig. 8 Normalized difference vegetation index.

In order to obtain the NDVI (normalized difference vegetation index) showed in Fig. 8, it was used data from the MODIS (moderate resolution imaging spectroradiometer) sensor aboard the TERRA satellite.

These data were compiled from the LP DAAC (land processes distributed active archive center) database of the USGS/EROS (Earth Resources Observation and Science) Center, Sioux Falls, and South Dakota

(http://lpdaac.usgs.gov/get_data). All data obtained from the satellite images were taken to a spatial resolution of 1 km. To initialize the meteorological variable profiles, it was used data obtained from a radio sounding in Ezeiza, corresponding to 12:00 UTC (9 a.m. local time) of January 1, 2011.

4. Results

Two simulation instances are compared versus the measured data of the weather stations. In the first simulation (case 1), it was not imposed the external boundary conditions, since it was used "radiative" conditions with value relaxation of meteorological variables at the initial state (sounding values in Ezeiza at 12:00 UTC). For the second simulation (case 2), it was imposed assimilated external conditions of MBLM. In Fig. 9, it can be observed the daily progress of wind direction at 10 m for the east, north and south towers, while Fig. 10 represents the same variable at 40 m. Fig. 11 shows the progress of wind speed at 10 m of height for the mentioned towers. Fig. 12 shows the same variable at 40 m. In these progresses, it can be observed the data measured by the anemometers with symbols, and the curves represent the results of simulations for cases 1 and 2.

In Fig. 13, it is shown the daily progress of air temperature at 2 m of height in the three towers, while Fig. 14 shows the progress of the same variable at 40 m. Tables 1 and 2 show the accuracy percentage of wind direction simulation regarding the recorded data at 10 m and 40 m. Table 1 considers "accuracy" when the simulated value reaches the recorded value quadrant, while Table 2 considers "accuracy" if the simulated value reaches the recorded values octant.

Fig. 15 presents a comparison between the recorded and simulated values (case 2) of wind speed at 10 m and 40 m for all the measurement towers, respectively. Fig. 16 also shows a comparison between recorded and simulation values (case 2) of air temperature at 2 m and 40 m, respectively.

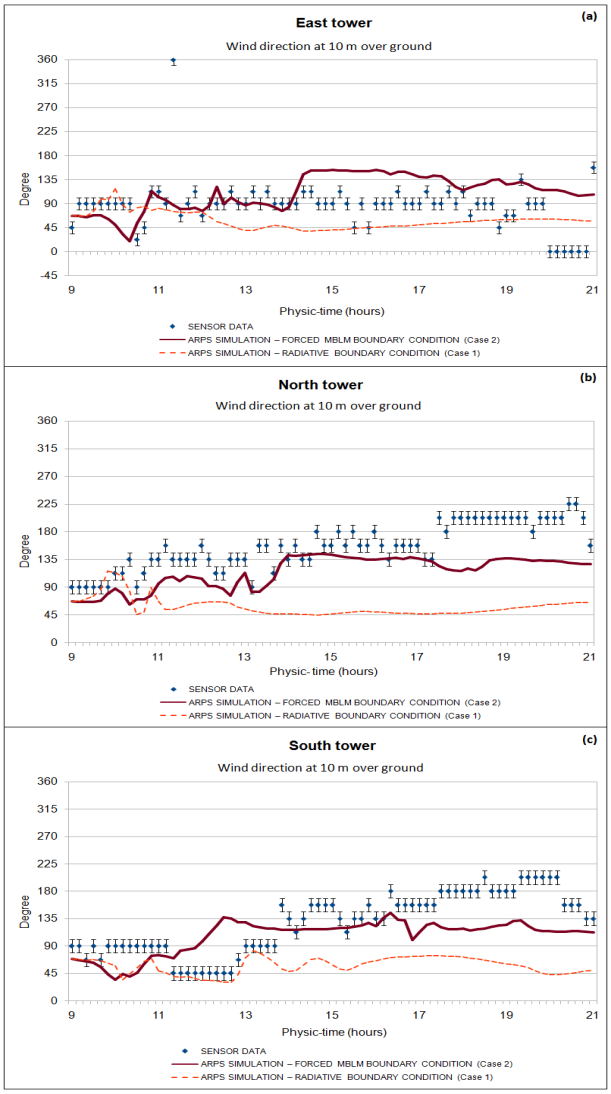

Fig. 9 Wind direction daily-progress at 10 m: (a) east tower; (b): north tower and (c) south tower.

5. Discussion

5.1 Wind Direction

One of the most important variables to simulate is wind direction; if it is well adjusted, it allows a better prediction of the plume trajectory of pollutant emissions and, consequently, a minor uncertainty in the delimitations of potential risk areas. Observing Figs. 9 and 10, it is important to highlight in first place, that from approximately 2 physical hours of simulation, simulated wind direction curves began to divide, having a better adjustment with the observed data in case 2, that is to say, using forced

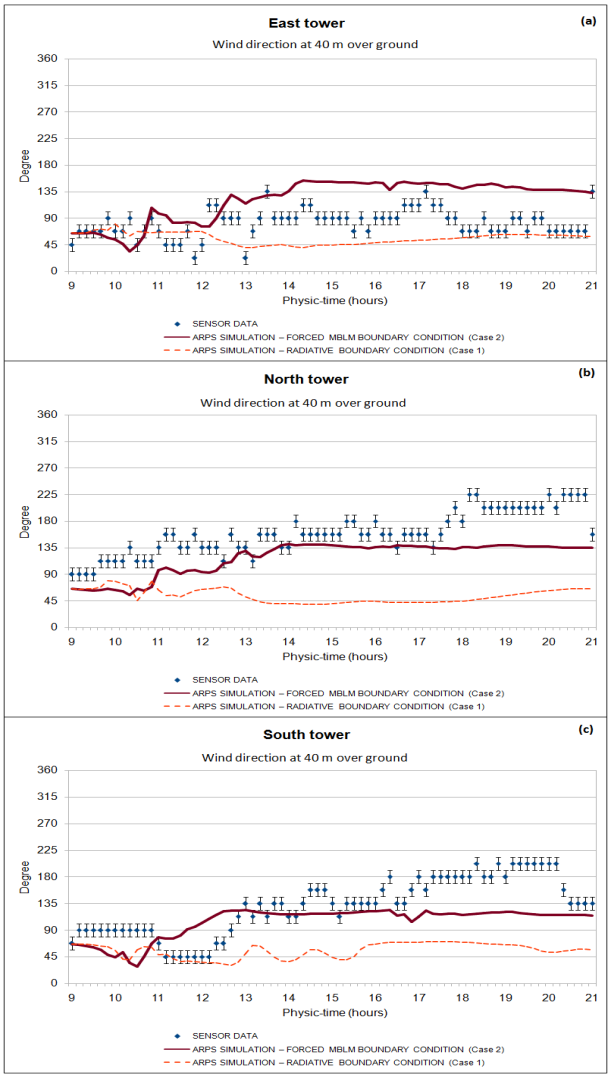

Fig. 10 Wind direction daily-progress at 40 m: (a) east tower; (b) north tower and (c) south tower.

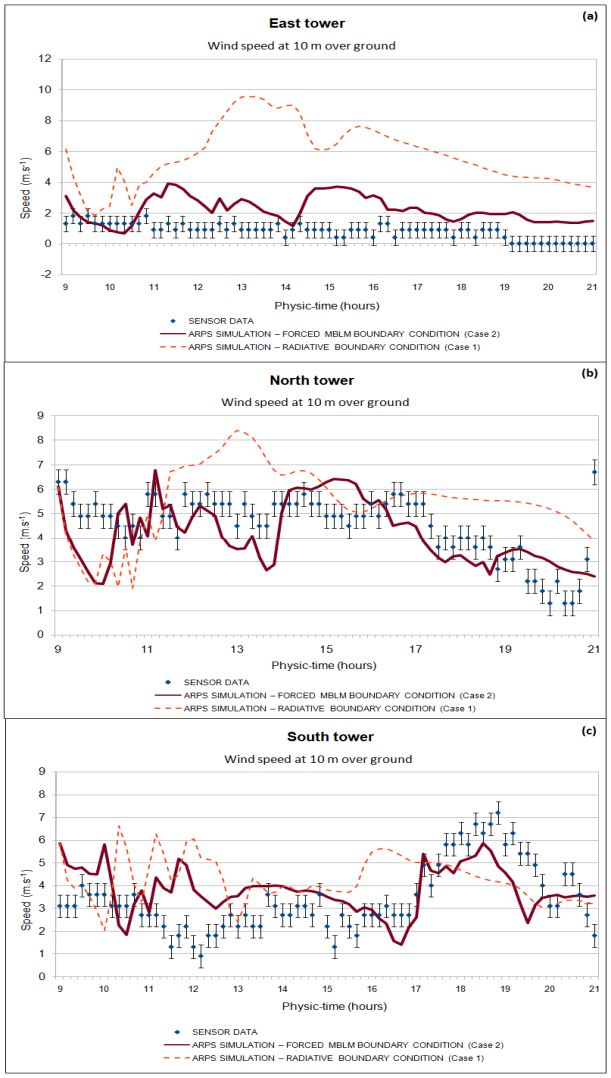

Fig. 11 Wind speed daily-progress at 10 m: (a) east tower; (b) north tower and (c) south tower.

boundary conditions from the results of MBLM. It is also observed that the progress corresponding to case 1 shows a wind direction that practically remains constant in 45°, which was expected since the imposed boundary conditions tend to be like the ones in initial state of the sounding in Ezeiza (NE wind).

Records of the stations show that the wind is from east and then rotates to south-south-east approximately at 11 a.m. in the north tower and at 2 p.m. in the south tower. These changes are acceptably simulated in the case of forced boundary conditions with the MBLM model between 2 p.m. and 6 p.m. After 6 p.m., wind keeps rotating to south in the north and south towers, but this is not well represented by the model.

Regarding the general adjustment for wind direction showed in Tables 1 and 2, it must be pointed out that they both achieved a substantial improvement in the prediction using the MBLM data (case 2) in relation to the use of "radiative" boundary conditions (case 1).

The adjustment by octant represents a lower accuracy percentage that the adjustment by quadrant, since for octant we have instrument error (the weather-vane records 16 directions of the compass rose). The quadrant analysis is more appropriate to analyze errors in this case of instrument. In both tables, it is noticed that for east tower, the accuracy percentage is higher than that in the other towers. This is because wind in that spot showed less direction

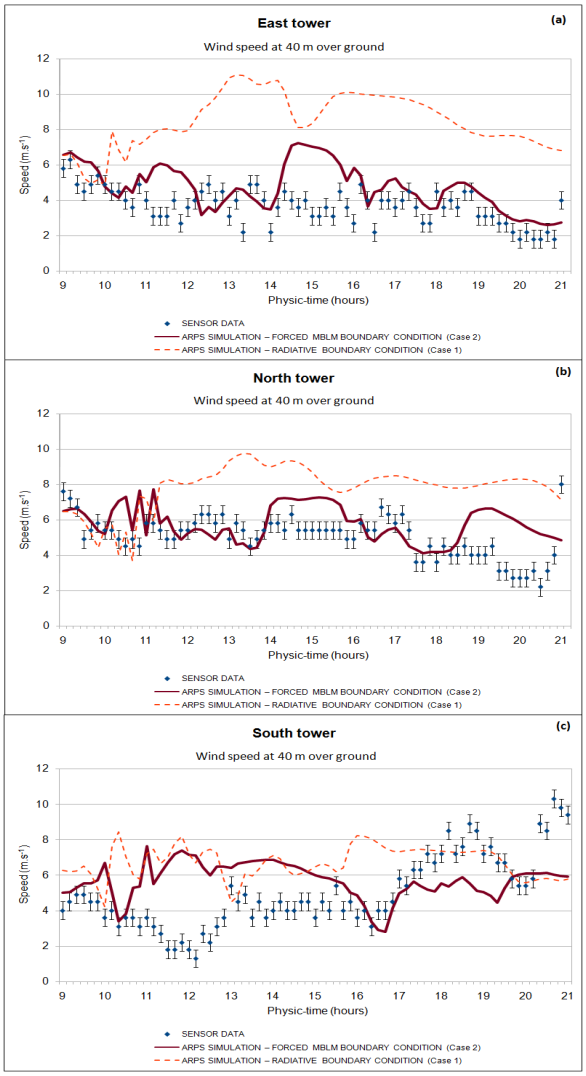

Fig. 12 Wind speed daily-progress at 40 m: (a) east tower; (b) north tower and (c) south tower.

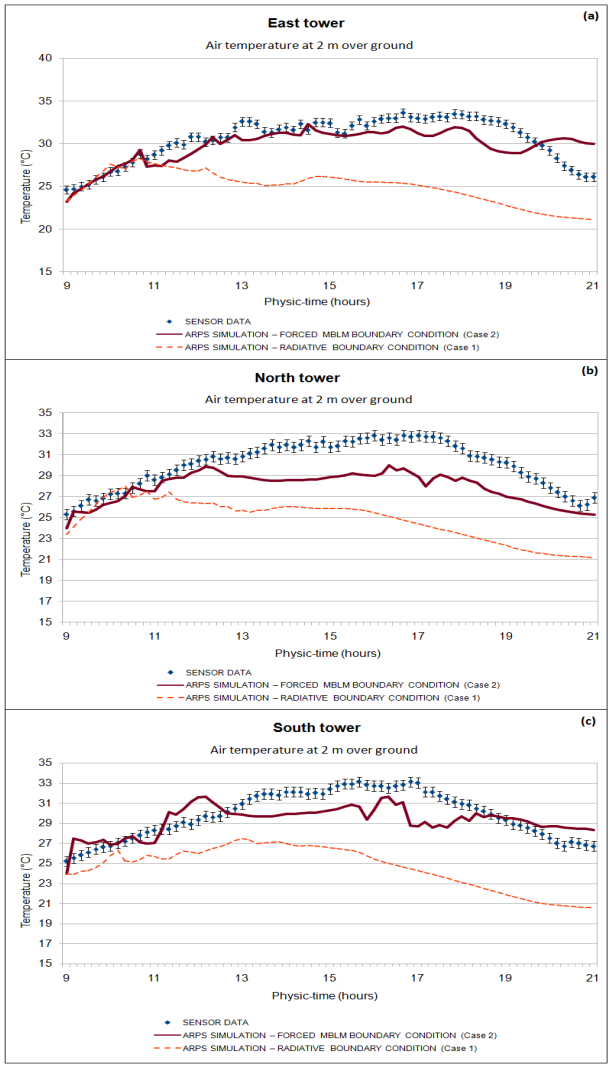

Fig. 13 Air temperature daily-progress at 2 m: (a) east tower; (b) north tower and (c) south tower.

variability for the entire simulation. In both tables, for all towers, it can be observed that there is a slight advantage at 10 m than at 40 m, except that in the octant analysis in south tower in case 2.

5.2 Wind Speed

Regarding wind speed, it can be observed in Figs. 11 and 12 that the forced model (case 2) represents this variable for all towers and both heights better than the one that use "radiative" conditions (case 1). At 10 m in east tower (Fig. 11a), recorded wind speed is very low, and though in both simulations (cases 1 and 2) they are overestimated, the ones corresponding to case 2 present a better adjustment than in case 1.

The comparison graphics shown in Fig. 15 (case 2) indicate that the simulations made at 10 m adjust better than the ones at 40 m. Particularly, in Fig. 15 corresponding to 10 m, the correlation coefficient R = 0.693, while at 40 m the correlation coefficient R = 0.217. Besides, the slope of the straight line of the linear regression in 10 m, is closer to the unit, while the ordinate at the origin is closer to zero. This indicated that in average for all towers, there is an overestimation of the wind speed value for lower values, and an underestimation for higher values. This model behavior was expected since we were comparing wind speed records obtained in a specific place, with values resulting from the large scales

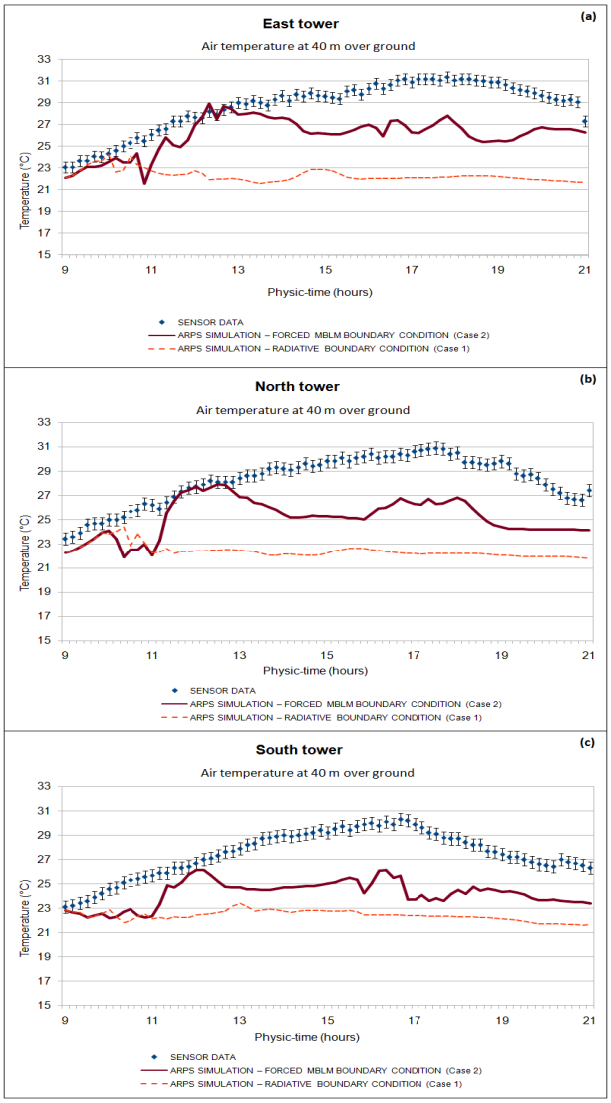

Fig. 14 Air temperature daily-progress at 40 m: (a) east tower; (b) north tower and (c) south tower.

Table 1 Accuracy percentage by quadrant.

	Case 1		Case 2	
	10 m	40 m	10 m	40 m
All towers	39.7	37.0	63.0	54.8
East tower	68.5	70.0	68.5	46.6
North tower	13.7	13.7	60.3	58.9
South tower	37.0	27.4	60.3	58.9

Table 2 Accuracy percentage by octant.

	Case 1		Case 2	
	10 m	40 m	10 m	40 m
All towers	18.3	18.3	29.7	27.9
East tower	21.9	42.5	34.2	20.5
North tower	6.8	0.0	31.5	28.8
South tower	26.0	12.3	23.3	34.2

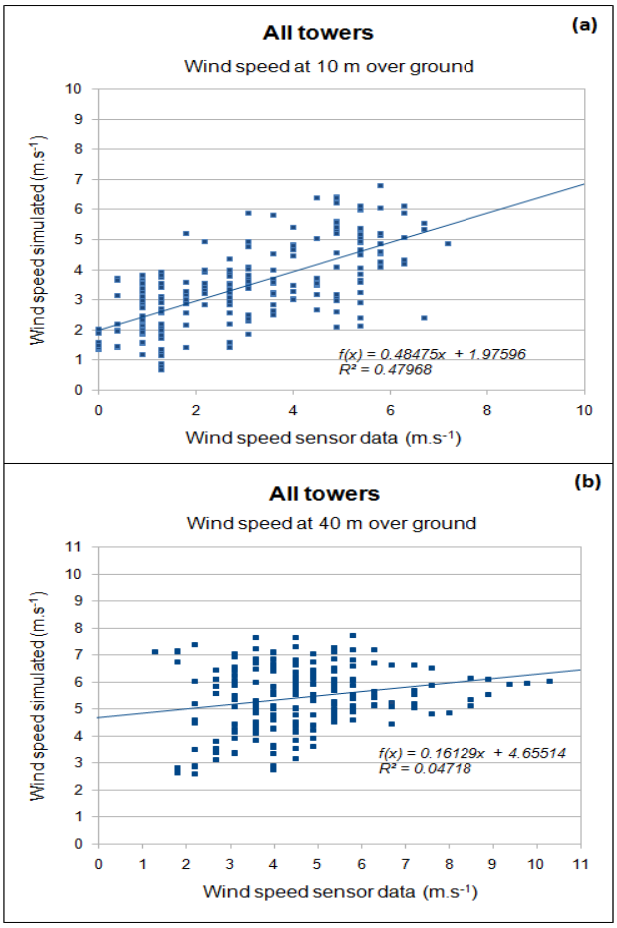

Fig. 15 Wind speed sensor data vs. simulated (case 2).

simulation of turbulence obtained with a low-pass filter, that is to say, a spatial average in a 1 km × 1 km cell. It should be obtained an improvement in the simulations for a reduction of the horizontal size of the calculation grid cells.

5.3 Air Temperature

In Figs. 13 and 14, it can be observed the daily progress of air temperature at 2 m and 40 m, respectively. The more pronounce thermal wave at 2 m is shown. Both simulations (cases 1 and 2) underestimate the recorded values in the towers, though, for case 2, the underestimation is lower than that in case 1. In Fig. 16, comparison graphics of temperatures in all towers at 2 m and 40 m show a general better adjustment than the ones in the simulation of speed wind. This might be because that temperature has a lower spatial variability than wind.

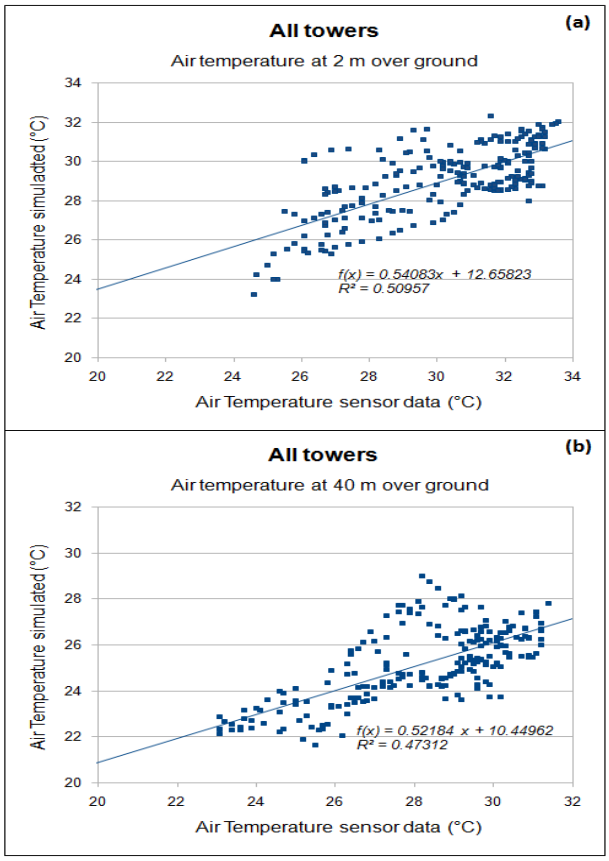

Fig. 16 Air temperature sensor data vs. simulated (case 2).

The adjustments in case 2, both at 2 m and 40 m, are quite similar, with a correlation coefficient $R = 0.714$ in the case of the simulation at 2 m, and of $R = 0.688$ in the case of simulation at 40 m. The slopes and ordinates to the origin of the linear regression equation are very similar, too, in both figures. These indicate that in average for all towers and both heights, the higher values are being underestimated, and the lower values of temperature are being overestimated, since the slopes are smaller than the unit and the ordinates to the origin are larger than zero. To explain this behavior, it can be applied the same reflection made for wind speed.

6. Conclusions

It is necessary to consider the changes of air circulation as forced boundary conditions when it is wanted to simulate wind direction and wind speed for a long time period of the order of days.

In the simulation of January 1, 2011, in the region of River Uruguay, nearby the city of Gualeguaychú, it is observed that a good adjustment of the wind direction quadrant, and a regular adjustment of speed in the instance of forcing the boundary conditions with data from the MBLM rather than the data recorded by the meteorological stations.

In the case of simulations obtained using "radiative" boundary conditions, the adjustment is not good after 2 h physical time of simulation. The recorded temperature at 2 m of height is slightly better simulated than at 40 m in the case of forced conditions with MBLM, but the adjustment in this simulation overtakes the one using "radiative" boundary conditions for both heights.

Acknowledgments

This research was made with the support of PICT2008-1417 and PICT2010-2492 projects, both of the National Agency for Science and Technology Promotion (ANPCyT).

ASTER L1B data were obtained from NASA LP DAAC database, USGS/EROS Center, Sioux Fall, and South Dakota (http://lpdaac.usgs.gov/get_data).

References

[1] Aguirre, C. A., Simoëns, S., and Ayrault, M. 2003. "Chemically Reactive Dispersion into Atmospheric Boundary Layer." Presented at the International Workshop on Physical Modeling of Flow and Dispersion Phenomena, Prato, Italy.

[2] Aguirre, C. A. 2005. "Eulero-Lagrangian Atmospheric Dispersion and Mixing of Reactive Fluid Particles. Aplication at Simple and Complex Cases." Ph.D. thesis, Claude Bernard Lyon 1 University.

[3] Aguirre, C. A., and Brizuela, A. B. 2008. "Numerical Simulation of Atmospheric Dispersion Gas passive over Hill Using a Coupled Model." *Serie Mecánica Computacional* 4: 217-37.

[4] Aguirre, C. A., Berri, G. J., Brizuela, A. B., and Orcellet, E. E. 2012. "Simulation of wind circulation and Temperature in Low Layers over the region of Gualeguaychú City, Argentina." *Serie Mecánica Computacional* 2: 21-36.

[5] Klemp, J. B., and Wilhelmson, R. B. 1978. "The Simulation of Three-Dimensional Convective Storm Dynamics." *J. Atmos. Sci.* 35: 1070-96.

[6] Berri, G. J. 1987. "Study of Thermo-Hydrodynamic Behavior of Atmospheric Boundary Layer over the region of Rio de la Plata with Numerical Simulation Model." Ph.D. thesis, Facultad de Ciencias Exactas y Naturales, UBA.

[7] Berri, G. J., Sraibam, L., Tanco, R., and Bertossa, G. 2010. "Low-Level Wind Field Climatology over the La Plata River Region Obtained with a Mesoscale Atmospheric Boundary Layer Model Forced with Local Weather Observations." *J. App. Meteorol. and Climat.* 49 (6): 1293-305.

[8] Xue, M., Droegemeier, K., and Wong, V. 2000. "The ARPS (Advanced Regional Prediction System). A Multi-Scale Nonhydrostatic Atmospheric Simulation and Prediction Model. Part I: Model Dynamics and Verification." *Meteorology Atmospheric Physics* 75: 161-93.

[9] Smagorinsky, J. 1963. "General Circulation Experiments with the Primitive Equations I. The Basic Experiments." *Mon. Weather Rev.* 91: 99-164.

[10] Germano, M., Piomelli, U., Moin, P., and Cabot, W. H. 1991. "A Dynamic Subgrid-Scale Eddy Viscosity Model." *J. of Physics Fluids* A 3: 1760-65.

[11] Leonard, A. 1974. "Energy Cascade in Large Eddy Simulation of Turbulent Fluid Flow." *Adv. Geophysics* 18A: 237-48.

[12] Deardorff, J. W. 1980. "Stratocumulus-Capped Mixed Layer Derived from a Three-Dimensional Model." *Boundary-Layer Meteorology* 18: 495-527.

[13] Proctor, F. H. 1987. *The Terminal Area Simulation System. Volume I: Theorical Formulation.* NASA contractor report.

[14] Olson, J. S., Watts, J. A., and Allison, L. J. 1985. *Major World Ecosystem Complexes Ranked by Carbon in Live Vegetation: A Database.* Oak Ridge: Oak Ridge National Laboratory.